Multi-index probabilistic anomaly detection for large span bridges using Bayesian estimation and evidential reasoning

Xiang Xu[1,2], Michael C. Forde[2], Yuan Ren[1], Qiao Huang[1] and Bin Liu[3]

Abstract

To measure uncertainties within anomaly detection and distinguish sensor faults from anomalous events, a multi-index probabilistic anomaly detection approach is proposed for large span bridges based on Bayesian estimation and evidential reasoning. To avoid false detection raised by signal spikes, an energy index is first defined and extracted from pre-processed measurements, including missing data recovery and thermal response separation. Then, a probabilistic index, namely certainty degree, is derived from probability density functions of detection triggers - extreme values predicted by using Bayesian estimation of the generalized Pareto distribution. To distinguish sensor faults from anomalous scenarios, evidential reasoning is applied to incorporate multiple certainty degrees into a joint one under the assumption that the probability of multi-sensor failing simultaneously is extremely low. Specifically, a large joint certainty degree indicates a high occurrence probability of anomalous scenarios, while a small one together with a large individual certainty degree depicts a high probability of sensor faults. Finally, the effectiveness of the proposed anomaly detection method is validated through structural health monitoring data from the Nanjing Dashengguan Yangtze River Bridge. Measurements from four sensors, i.e., three cable forces and one deflection, are selected to detect anomalies based on their high pair-wise correlations. Two case studies are presented, namely sensor fault detection and snow disaster detection. The sensor fault is detected through a certainty degree of almost 100% for the individual index and a joint certainty degree of nearly 0. The snowstorm is detected by a joint certainty degree of 36.82%.

Prepared using **sagej.cls** *[Version: 2017/01/17 v1.20]*

Introduction

Prognostic health monitoring is a mechanism of preventive measures to deliver comprehensive and tailored solutions for the industrial health system, management, and prediction[1,2]. In civil engineering, structural health monitoring (SHM) systems are often applied to large-scale civil infrastructures, especially large span bridges, to measure environmental factors, external loads, and structural responses[3–5].

Based on measurements from SHM systems, anomaly detection for large span bridges has been broadly studied all over the world within recent decades. Modal parameters (e.g., curvature mode shapes) were explored to detect structural damages relying on their sensitivities to defects such as drops in stiffness[6–8]. Although their effectiveness was theoretically and experimentally validated, challenges emerged when applied to practical applications owing to the contamination of signal noises and impact of environmental variations[9]. For instance, fluctuations of dynamic characteristics caused by temperatures were larger than those induced by structural damages for a cable-stayed bridge[10].

In addition to dynamic responses, scholars explored to take advantages of static responses (e.g., strains) to detect anomalies. Yu et al.[11] used girder deflection measurements from a beam bridge to detect damages via wavelet transform and Lipschitz exponent. Hua et al.[12] considered variations of cable forces to detect damages for a cable-stayed bridge under the rationale that damages induced a force redistribution in stay cables. Similar to dynamic fingerprints, environmental factor, especially temperatures, is a major interference in anomaly detection by using static responses.

Methodologies associated with thermal effect modelling and separation were well studied in recent years, such as regression models[13,14], wavelet transform[15,16], blind source separation[17], numerical models[18,19], Bayesian models[20,21] and so forth. In view of the impact of thermal effects, temperature-driven anomaly detection techniques were increasingly

[1]School of Transportation, Southeast University, Nanjing 210 096, China
[2]School of Engineering, University of Edinburgh, Edinburgh EH8 9YL, UK
[3]Department of Management Science, University of Strathclyde, Glasgow F1 1XQ, UK

Corresponding author:
Xiang Xu, School of Engineering, University of Edinburgh, Edinburgh EH8 9YL, UK.
Email: xxuseu@126.com

developed. Xu et al.[22] established a two-level anomaly detection framework using mid-span deflection measurements from a large span suspension bridge, where the multi-resolution wavelet-based method was used to separate thermal responses. Zhu et al.[23] improved the efficiency of moving principal component analysis for anomaly detection by introducing blind source separation to identify thermal strains. Tome et al.[24] and Fan et al.[25] presented a damage detection strategy for a large cable-stayed bridge, where the environmental effects were suppressed using cointegration. Huang et al.[26] proposed a strain-based anomaly detection method, where the correlation model between main girder strains and temperatures was built up.

Furthermore, existing anomaly detection methodologies were mostly in the deterministic context, dismissing the inherent uncertainty within the detection course[27]. However, uncertainties are inevitably involved in the detection process induced by environmental variability, measurement noises and parameter estimation. In this regard, probabilistic approaches are preferable in detecting anomalies for large span bridges. Bayesian inference, a powerful tool in dealing with uncertainties, has been increasingly adopted to quantify uncertainties in engineering fields. Ni et al.[21] took advantages of expansion joint displacements to detect damages under the Bayesian context, where in-situ measurements from a cable-stayed bridge were employed to validate the effectiveness of the proposed method. Yu and Cai[28] introduced Bayesian methods to predict extreme structural responses subject to traffic loads to improve the reliability of bridge condition assessment, where measurements from the new I-10 twin span bridge were used to verify the effectiveness of the proposed method. Xu et al.[29] applied Bayesian estimation to extreme value analytic to estimate probabilistic distributions of site-specific extreme loads for a cable-stayed bridge. Therefore, Bayesian inference is a promising way to address the uncertain issue within the anomaly detection process.

However, owing to inefficient manufacture, harsh operation environment and performance degradation, sensor faults are evolving as an increasing concern in anomaly detection and condition assessment techniques[30]. Most existing anomaly detection methods were carried out with the assumption that the studied sensors were all in working order. However, anomaly detection is often falsely triggered by sensor faults rather than anomalous scenarios in practice. On the other hand, studies

regarding sensor fault diagnosis were also well investigated, which took root in the redundancy of information. Based on the source of redundant information, two types of methods are defined, namely the model-based and data-driven. The model-based method uses the redundancy provided by mathematical models, while the data-driven relies on the monitored data from remaining or extra sensors[31]. Within existing sensor fault diagnosis, the structure was usually assumed to be intact, however, there could be a scenario that both structural damages and sensor faults coincide resulting in a coupling problem[32]. Currently, anomaly detection in civil engineering detects general anomalous signals, including sensor faults and structural damages[33,34]. However, sensor faults and structural damages are subject to different coping strategies, respectively. For structural damages, a prompt inspection is necessary to ensure the structural and operational safety of the bridge. For sensor faults, a replacement plan should be made, whose priority is much lower than that of structural damages. In this regard, distinguishing sensor faults from structural damages will help owners to make proper maintenance decisions. To the best of the authors' knowledge, rare investigation has been carried out for anomaly detection of large span bridges considering the interference of sensor faults[31,33,34].

In this study, a multi-index probabilistic anomaly detection approach for large span bridges will be developed under the context of Bayesian inference and evidential reasoning. Multiple static responses are first selected for anomaly detection based on their pair-wise correlations. To avoid the influence of spikes, an energy index is proposed within a determined time window. Then, the generalized Pareto distribution (GPD), one of extreme value analysis tools, is adopted to estimate probabilistic distributions of detection triggers, where Bayesian estimation is used to calculate probability density functions (PDFs) of triggers. Subsequently, a probabilistic index, certainty degree, is derived from PDFs of triggers to rate uncertainties. To resolve the coupling between sensor faults and anomalous scenarios, evidential reasoning is employed to incorporate multiple certainty degrees into a joint one. Finally, the effectiveness of the proposed anomaly detection method is verified through measurements from a large span cable-stayed bridge.

Methodology of multi-index probabilistic anomaly detection

The general flowchart for the multi-index probabilistic anomaly detection is presented in Figure 1. Measurements of multiple sensors are collected from SHM systems to detect anomalies based on their pair-wise correlations. Missing data are filled to enhance the signal continuity[35,36]. Thermal compensation is completed to separate thermal responses[15,37]. Once obtaining the pre-processed signals, energy index is extracted to achieve robust detection performance, where two parameters (i.e., length of window and number of overlaps) need to be determined. Based on relatively long-term energy indices, thresholds for the GPD analysis are determined. Bayesian estimation is employed to figure out PDFs of detection triggers, and a probabilistic index, certainty degree, is derived from PDFs to measure uncertainties. To address the coupling between sensor faults and anomaly scenarios, evidential reasoning is used to incorporate multiple certainty degrees into a joint one. It is assumed that the probability of multi-sensor failing simultaneously is extremely low since each sensor operates independently, while the anomalous scenario always triggers multiple indices at the same time owing to the redundancy between sensors. In this regard, although the sensor fault might lead to a high certainty degree of a single index, the joint certainty degree will stay at a relatively low level since the other indices are not triggered. On the other hand, the anomalous scenario is subject to a relatively high joint certainty degree since most of the indices are triggered.

Data collection and pre-processing

Most of existing literature associated with static index-based anomaly detection methods focused on a single index, such as strains[23], deflections[22] and cable forces[25]. Compared with the single index-based anomaly detection, the multi-index anomaly detection has potential to detect anomalies as more as possible. In practice, various sensors are devised to monitor environmental factors, external loads, and structural responses, providing a data foundation for the multi-index anomaly detection. However, the multiple indices should be selected carefully to achieve the goal to distinguish sensor faults from anomalous scenarios. As discussed, sensor fault detection relies on redundant information. If the selected indices are all independent from each other, it is natural that the detection result of each index is discrepancy. In this regard, the evidential
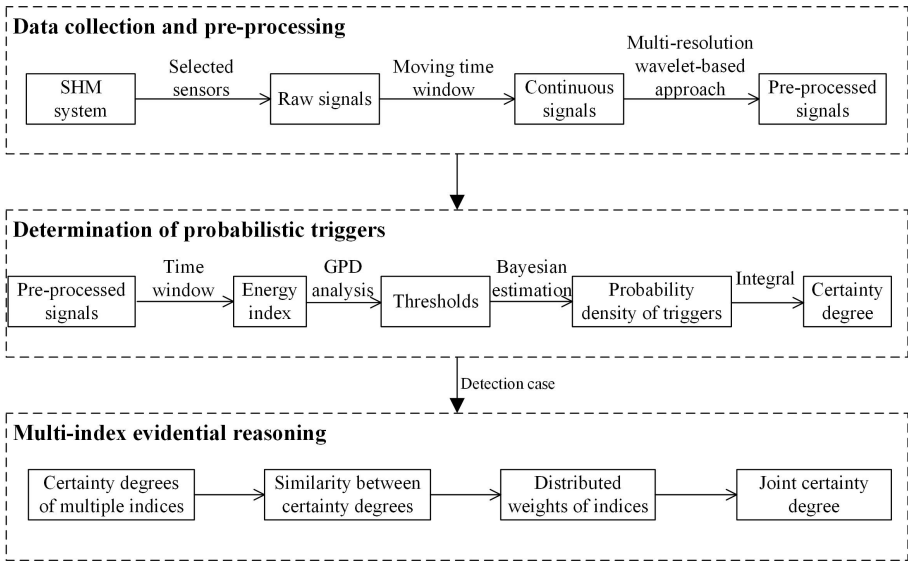
Figure 1. Flowchart of the multi-index probabilistic anomaly detection method, including data collection and pre-processing, determination of probabilistic triggers, and multi-index evidential reasoning.

reasoning is unnecessary, and it is impossible to distinguish sensor faults from anomalous scenarios due to lack of redundant information. Thus, prior to carrying out multi-index anomaly detection, high correlated multiple indices should be selected to provide redundant information. Based on experience, the indices responding to outer actions accordingly will have a relatively high correlation. For example, the cable force and deflection around mid-span area will have relatively strong correlation since they all yield to the mid-span girder deformation.

In general, the correlation is indicated by the scale of Pearson correlation coefficient (R) as: very high correlation ($0.8 \le |R| \le 1.0$), High correlation ($0.6 \le |R| < 0.8$), moderate correlation ($0.4 \le |R| < 0.6$), low correlation ($0.2 \le |R| < 0.4$), and very low correlation ($0 < |R| < 0.2$). If the correlation standard is set too high, few indices are qualified for the multi-index anomaly detection. In contrast, if the standard is set too low, the redundant information among the selected indices is not enough to distinguish sensor faults from anomalous scenarios. In this regard, the determination of correlation threshold is a trade-off problem.

In this study, we set the threshold as high correlation ($|R| \geq 0.6$) for the correlation analytic.

Before detecting anomalies, signals are required to be pre-processed to improve their quality. Existing missing data recovery methods include moving time window mean imputation[38], maximum likelihood[39], artificial neural networks[40] and Bayesian inference approach[41]. In this study, since a small portion of discrete data are missed, the moving time window mean imputation is adopted herein[38].

Thermal effect is not the response of interest for anomaly detection, which may cover signal fluctuations induced by anomalous events. Herein, the multi-resolution wavelet-based method is applied to separate thermal responses from the recorded data[15].

Determination of probabilistic triggers

Index extraction Spike is a common issue in measured SHM data, generated from capacitive or inductive noise in the analogue signal and communication errors in asynchronous communication protocols[42]. In general, the spike within signals is non-physical event with an amplitude of at least twice that of the background activity, and a short duration of $\leq 200ms$. The spike will introduce false detection in the single signal-based anomaly detection since the amplitudes of spikes further exceed the defined anomaly detection triggers[43].

To achieve robust performance in anomaly detection, an energy index in time domain is extracted from the measured data in this study[22]. The index is defined as the average energy within a determined time window, which is expressed as

$$I_d(i) = \begin{cases} \frac{\sum_{t=1}^m x^2(t)}{m}, & i = 1 \\ \frac{\sum_{t=(i-1)m+1-p}^{mi-p} x^2(t)}{m}, & i > 1 \end{cases} \tag{1}$$

where $x(t)$ is the time history, m is the length of window, and p is the number of overlaps. Compared with single signal-based indices, the energy index extracts the feature from a determined time window to achieve peak clipping, which in theory has higher tolerance for signal spikes.

GPD analysis In general, the trigger is supposed to be the extreme value of the defined index under normal operational circumstances[44]. The block

maxima method was often used to predict extreme values[45], however, only annual maxima are adopted for the extreme value estimation in the block maxima method. Considering the limited available monitored data, the GPD is used to estimate extreme values of indices, which has a more efficient data utilization rate[46].

The GPD is a family of continuous probability distributions, which are often used to model the tails of another distribution via peak-over-threshold technique[47]. The energy index $I_d(i)$ is supposed to obey a certain distribution. The tails of $\vec{I_d}$, i.e., the excess $s(i) = I_d(i) - u_0$, are modelled by the GPD, where u_0 is the threshold and $s(i) > 0$. The cumulative density function of the GPD subject to an excess $s(i)$ takes the form[22]

$$G(s(i); \sigma, \xi) = \begin{cases} 1 - (1 + \xi\frac{s(i)}{\sigma})^{-1/\xi}, & \xi \neq 0 \\ 1 - \exp\left(-\frac{s(i)}{\sigma}\right), & \xi = 0 \end{cases} \tag{2}$$

where σ is the scale parameter, and ξ is the shape parameter. The corresponding PDF is

$$g(s(i); \sigma, \xi) = \frac{1}{\sigma}(1 + \frac{\xi s(i)}{\sigma})^{-1-1/\xi} \tag{3}$$

for $s(i) \geq 0$ when $\xi > 0$, and $0 \leq s(i) \leq -\sigma/\xi$ when $\xi < 0$. When $\xi = 0$, the PDF is

$$g(s(i); \sigma, \xi) = \frac{1}{\sigma}exp(-\frac{s(i)}{\sigma}) \tag{4}$$

for $s(i) \geq 0$.

The basic steps to determine probabilistic detection triggers by using the GPD are as follows:

I Re-sampling: To determine triggers by using the GPD, samples are required to be independently and identically distributed[47]. In this paper, maxima of the energy index within 24 hours are adopted for further discussions.

II Threshold: It is a crucial step to set an appropriate threshold. If the threshold is set too high, the number of out-of-samples is small, resulting in statistical uncertainty. On the other hand, if the threshold is too low, the excess quantity differs significantly from the maximum value, leading to a biased estimator. The mean excess

function of the GPD is introduced herein to determine a proper threshold, which is[48]

$$e(u) = \frac{1}{N_u} \sum_{i=1}^{N_u} [I_d(i) - u]$$

$$= \frac{\xi}{1 - \xi} u + \frac{\sigma}{1 - \xi} \tag{5}$$

in which N_u denotes the number of excesses over the threshold, and u is the threshold. The mean excess function is supposed to be a linear function of the excess quantity. However, the transition from the curve to the straight line is not a point but an interval. To overcome this shortcoming, the root mean square error (RMSE) is introduced as

$$RMSE = \sqrt{\frac{\sum [e(u) - L_e(u)]^2}{n}} \tag{6}$$

where $L_e(u)$ is the linear fit of the mean residual life above the threshold, and n is the number of candidate thresholds. The minimum value of RMSE indicates the best linear fit of mean residual life and threshold, which corresponds to the optimal threshold.

III Parameter: According to the daily maxima, the posterior distributions of scale and shape parameters can be estimated by using Bayesian estimation. One can refer to next section for detailed descriptions.

IV Trigger: The extreme value subject to a certain quantile is regarded as the trigger for anomaly detection. Within the reference period of T years, the cumulative probability p corresponding to an exceedance probability rate P_r is

$$p = 1 - \sqrt[T]{P_r} \tag{7}$$

The trigger for anomaly detection is expressed as

$$T_a = u_0 + \frac{\hat{\sigma}}{\hat{\xi}} \{ [\frac{N_{total}}{N_u} (1 - p)]^{-\hat{\xi}} - 1 \} \tag{8}$$

where u_0 is the threshold, $\hat{\sigma}$ is the estimated scale parameter, $\hat{\xi}$ is the estimated shape parameter, N_{total} is the number of all samples, and N_u is the number of excesses. Generally, the trigger is defined as the

244   quantile value corresponding to the 95% guarantee rate within a 100-
245   year reference period (i.e., a return period of 1950 years), which is in
246   line with the design code.

247   V Certainty degree: Since the uncertainty of scale and shape
248   parameters, the potential triggers will vary and follow a certain
249   distribution, termed as $T_a \sim f(\alpha, \beta)$, where α and β are the
250   parameters defining the distribution. Given the value of an index
251       $I_d(i)$, the certainty degree for occurrence of an anomalous scenario
252   is

$$m_i = \int_{T_a=0}^{I_d(i)} f(T_a; \alpha, \beta) dT_a \tag{9}$$

253 **Bayesian estimation** Bayesian estimation is adopted in this study to
254 measure uncertainties of the predicted triggers. Based on Bayes' theorem,
255 the posterior distribution of the parameters is[21]

$$p(\vec{\theta}; \vec{s}) = \frac{L(\vec{\theta}; \vec{s})p(\vec{\theta})}{\int L(\vec{\theta}; \vec{s})p(\vec{\theta})d\vec{\theta}} \tag{10}$$

256

$$L(\vec{\theta}; \vec{s}) = \prod_{i=1}^{N_u} g(s(i); \vec{\theta}) \tag{11}$$

257 where $\vec{\theta}$ is the parameter vector of the GPD, $\vec{s}$ is the excess vector, $p(\vec{\theta}; \vec{s})$
258 is the posterior distribution of the parameter vector, $p(\vec{\theta})$ is the prior
259 distribution, $L(\vec{\theta}; \vec{s})$ is the likelihood function, $g(s(i); \vec{\theta})$ is the PDF of
260 the GPD, $s(i)$ is the ith excess, and N_u is the number of excesses.
261   Under Bayesian inference, the prior distribution indicates prior
262 knowledge regarding the parameters, which is independent from existing
263 observations. Since litter or no prior knowledge is known, a flat
264 distribution is used.
265   The Markov Chain Monte Carlo (MCMC) sampling can obtain the
266 posterior distribution of the GPD parameters. Herein, the Metropolis-
267 within-Gibbs (MG) sampler is employed, and the specific steps could refer
268 to the reference[49].
269   After a period of iterations, the Markov chain converges to a stationary
270 distribution. The period of iterations before the Markov chain convergence
271 is called the burn-in period. The simulated values in the burn-in period

cannot be treated as samples to form the posterior distribution. Excluding the burn-in period, the remaining chain is used to discuss the stochastic characteristics of the posterior distributions.

The posterior distribution of the predicted triggers in theory is

$$p(T_a - u_0; \vec{s}) = \int g(T_a - u_0; \vec{\theta}) p(\vec{\theta}; \vec{s}) d\vec{\theta} \tag{12}$$

where T_a is the predicted trigger, g is the PDF of the GPD, and p is the posterior distribution of the GPD parameters. In practice, the posterior distribution of triggers is generated by using the following procedure:

I For $i = 1 : M$, given the parameters from the posterior distributions, a sample of triggers is calculated according to equation (8).

II Repeat step 1 until i reaches M, the obtained samples will be a realization of size M from the posterior distribution of predictive triggers.

Multi-index evidential reasoning

Evidential reasoning is one of the most used decision-making tools to deal with uncertain problems caused by randomness and fuzziness without prior probability and conditional probability density[50,51]. However, the conventional Dempster-Shafer evidence theory has limitations in dealing with conflicts[52,53]. To overcome such drawbacks, scholars put forward various improved methodologies. In general, existing methods can be classified into two categories: (1) one is to modify the classic combination rules of evidence theory to relocate conflicts[54]; and (2) the other is to modify the conflicted evidence before fusion without changing the combination rules[55]. Nevertheless, existing evidence research ignores to rate conflict degrees of evidence, which is supposed to be prior before the fusion of conflicted evidence.

In the context of multi-index anomaly detection system, each detection index reflects system status in its own way. Conflicts between indices lead to difficulties for decision-makings. Yet on the other hand, each single index has its own limitations in anomaly detection owing to its limited information. While a joint index, derived from multiple indices, can achieve a more robust anomaly detection performance. Herein, evidential reasoning is determined as the fusion operator based on
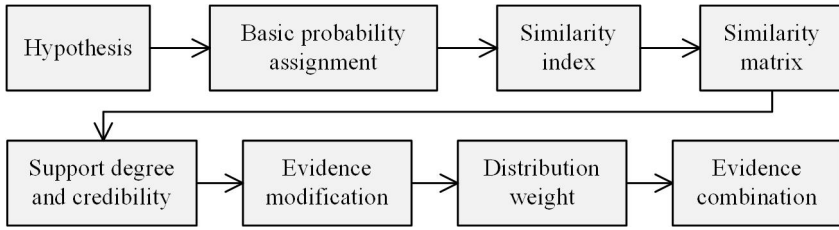
Figure 2. General steps of multi-index combination using evidential reasoning based on evidence similarities.

evidence similarities, and the specific steps for multi-index combination are shown in Figure 2.

It is assumed that the probability of multi-sensor failing simultaneously is extremely low since each sensor operates independently, while the anomalous scenario always triggers multiple indices at the same time owing to information redundancy. In this regard, although the sensor fault might lead to a high certainty degree of a single index, the joint certainty degree will stay at a relatively low level since the other indices are not triggered. On the other hand, the anomalous scenario is subject to a relatively high joint certainty degree since most of the indices are triggered. Three detection modes are summarized as follows

Mode I Normal state - Both individual and joint indices are 0 or extremely low.

Mode II Sensor fault - Relatively high single individual index together with a relatively low joint index, and the faulty sensor is subject to the relatively high single index.

Mode III Anomalous event - Multiple relatively high individual indices and relatively high joint index.

The specific steps to determine the joint occurrence probability of anomalous behavior are listed as follows:

I Suppose there are N pieces of independent evidence. In this paper, the framework of identification Γ is set as

$$\Gamma = [\gamma_1, \gamma_2] \tag{13}$$

where γ_1 represents anomalous event, and γ_2 stands for normal event.

II If $A_k \subseteq \Gamma$, and the function $m(A_k)$ satisfies the conditions $m(\emptyset) = 0$
and $\sum_j m(A_k) = 1$, m is the basic probability assignment (BPA)
function within Γ, and $m(A_k)$ is termed as the BPA for A_k, indicating
the support degree of the evidence to the proposition A_k in the
framework of identification. If $m(A_k) > 0$, then A_k is termed as a
focal element. The union of all the focal elements of the evidence
is termed as the nucleus $\mathbf{G}$ of the evidence and the evidence is
expressed as $(\Gamma, \mathbf{G}, m)$. The BPA function is the certainty degree
defined in equation (9). N pieces of evidence are expressed as

$$\begin{aligned}
E_1 &: [m_1(A_1), m_1(A_2), m_1(\Gamma)] \\
E_2 &: [m_2(A_1), m_2(A_2), m_2(\Gamma)] \\
&\quad ... \\
E_N &: [m_N(A_1), m_N(A_2), m_N(\Gamma)]
\end{aligned} \tag{14}$$

where $m(A_1)$ is the certainty degree subject to the proposition of
anomalous event, $m(A_2)$ is that of the normal condition, and $m(\Gamma)$ is
the certain degree that both anomalous event and normal event could
happen. In general, A_k is composed with one, multiple, or all γ_k.
However, in this case, $A_k = \gamma_k$.

III The similarity between two pieces of evidence is rated by using

$$r(m_i, m_j) = \frac{\sum_{k=1}^{N_A} m_i(A_k) m_j(A_k)}{\sum_{k=1}^{N_A} m_i(A_k)^2 + m_j(A_k)^2 - \sum_{i=1}^{N_A} m_i(A_k) m_j(A_k)} \tag{15}$$

where N_A is the number of focal elements. The similarity of
the evidence is between 0 and 1. A larger value indicates higher
similarity.

IV Once obtaining the similarities between each two pieces of evidence,
a $N \times N$ dimensional similarity matrix $\mathbf{R}$ is built as

$$\mathbf{R} = \begin{bmatrix} 1 & r(m_1, m_2) & ... & r(m_1, m_N) \\ r(m_2, m_1) & 1 & ... & r(m_2, m_N) \\ \vdots & \vdots & \ddots & \vdots \\ r(m_N, m_1) & r(m_N, m_2) & ... & 1 \end{bmatrix} \tag{16}$$

V The degree of support $S(m_i)$ on evidence i from all the other evidence is

$$S(m_i) = \sum_{j=1, j \neq i}^{N} r(m_i, m_j) \tag{17}$$

The credibility of evidence is the normalized value of the support degree. The credibility of the evidence i, C_i, is described as

$$C_i = \frac{S(m_i)}{\max[S(m_i)]} \tag{18}$$

VI Use the credibility C_i as the weight of evidence and correct the BPA function. Considering the condition of $\sum_i m(A_k) = 1$, the updated BPA function should follow the critetion as[50]

$$\hat{m}_i(A_k) = \begin{cases} C_i m_i(A_k), & A_k \neq \Gamma \\ C_i m_i(A_k) + (1 - C_i), & A_k = \Gamma \end{cases} \tag{19}$$

VII The relative credibility D_i for evidence i is

$$D_i = \frac{S(m_i)}{\sum_{i=1}^{N} S(m_i)} \tag{20}$$

The distribution weight of focal element A is[50]

$$\delta(A, \hat{m}) = \sum_{i=1}^{N} D_i \hat{m}_i(A) \tag{21}$$

VIII The final fusion results are derived by applying the combination operator as[50]

$$m(A) = \begin{cases} 0, & A = \emptyset \\ \sum_{\cap A_k = A} \prod_{1 \leq i \leq N} \hat{m}_i(A_k) + K\delta(A, \hat{m}), & A \neq \emptyset \end{cases} \tag{22}$$

in which K is the coefficient to evaluate the conflict of the modified evidence model, which is calculated by[50]

$$K = \sum_{\cap A_k = \emptyset} \prod_{1 \leq i \leq N} \hat{m}_i(A_k) \tag{23}$$
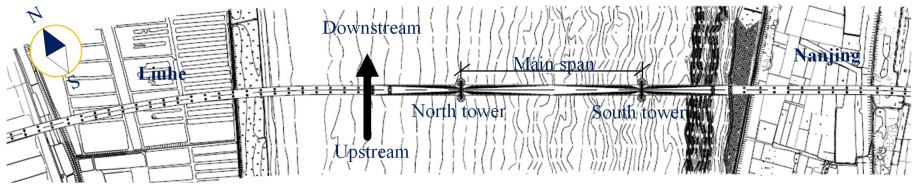
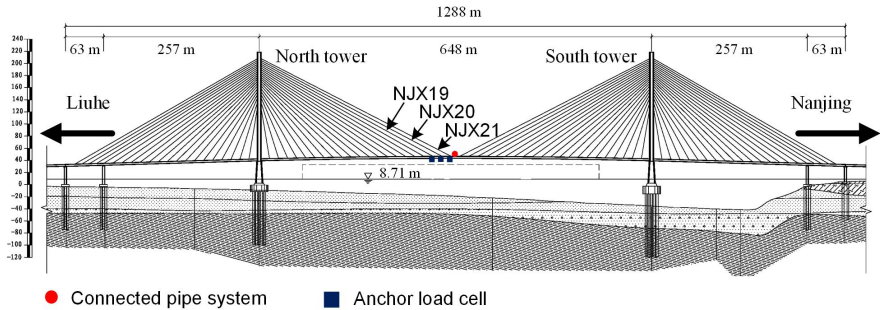**Figure 3.** Site plan of the Nanjing Dashengguan Yangtze River Bridge.

Figure 4. Configuration and sensor layout of the Nanjing Dashengguan Yangtze River Bridge.

Case study

The Nanjing Dashengguan Yangtze River Bridge (NDB) and its SHM system

The NDB, a vital transportation link, crosses the Yangtze River and connects Liuhe District with Nanjing City as shown in Figure 3. The steel cable-stayed bridge has a total length of 1288m, where the main span is 648m. The configuration of the NDB is shown in Figure 4. The bridge deck is supported by a total of 168 stay cables, and each cable consists of 109 to 241 wires of a 7mm diameter.

A SHM system was devised and installed to monitor the environmental factors, external loads and structural responses in the second year after the completion of the bridge in 2005. A total of 599 sensors were employed, including anemometers, temperature sensors, anchor load cells, connected pipe system and others. Forces of all the 168 stay cables are recorded by using the JC1-type anchor load cells with a sampling frequency of 10Hz and a relative measurement error of ±1%. The girder deflections

Table 1. Pairwise correlation coefficients for the four indices, i.e., forces of stay cable NJX21, NJX20, NJX19 and mid-span deflection.

Correlation coefficient	NJX21	NJX20	NJX19	Mid-span deflection
NJX21	1	0.9547	0.8292	0.8009
NJX20	0.9547	1	0.9541	0.8786
NJX19	0.8292	0.9541	1	0.8958
Mid-span deflection	0.8009	0.8786	0.8958	1

are measured using the Rosemount 3051S connected pipe system with an acquisition frequency of 10Hz and a resolution of ±1.5mm.

The selected indices for multi-index anomaly detection not only are close in space but respond similarly to outer actions. The candidate indices, namely forces of stay cables NJX21, NJX20, NJX19 and mid-span deflection as highlighted in Figure 4, are selected in advance, whose measurement locations are relatively close, concentrating on the middle span area. Owing to the slight difference between their measurement locations, means in 20 seconds are used to calculate the correlation coefficients to depict the similarity of their responses. The correlation coefficients are calculated and listed in Table 1 using one hour data. The measurements from the selected four sensors are highly pair-wise correlated, where the highest correlation coefficient equals to 0.9547 for NJX20 and NJX19, while the lowest one is 0.8009 for NJX21 and mid-span deflection. In this paper, measurements of the stay cables NJX21, NJX20, NJX19 and mid-span deflections are adopted as anomaly detection indices for the following anomaly detection analysis.

Data pre-processing

Raw measurements from the studied four sensors in 10 seconds are plotted in Figure 5(a). The data missing phenomenon was observed in the cable force signals, while deflection signals have a relatively good continuity. The moving time window mean imputation is employed to address the data missing issue with a window length of 2 seconds. After missing data recovery, the signals achieve a good continuity as shown in Figure 5(b).

Signals of the stay cable NJX21 in 24 hours, as shown in Figure 6(a), are taken as the example to explain the thermal separation procedure using the multi-resolution wavelet-based approach. The decomposition level is set as 27, and the wavelet basis function is 'coif5' in this study. The daily thermal effects were estimated to lie in the 19th detail level,
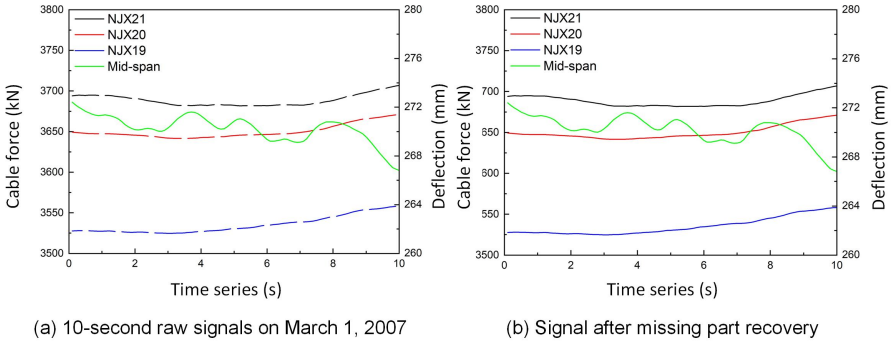
(a) 10-second raw signals on March 1, 2007   (b) Signal after missing part recovery

Figure 5. Missing data recovery process for the cable force and deflection data.

(a) 24-hour cable forces and temperature   (b) Signals after thermal response separation
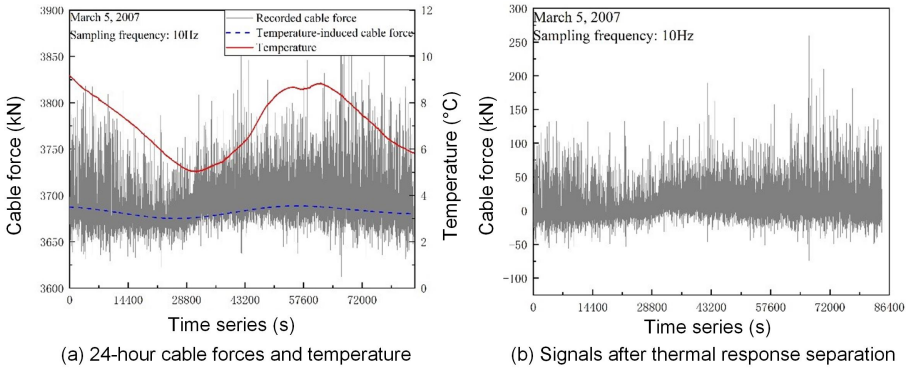
Figure 6. Thermal response separation process for the measurements from stay cable of NJX21.

and the seasonal ones were located at the 27th approximation level. The extracted temperature-induced cable forces are plotted in Figure 6(a), whose variation trend is in line with that of the temperatures. Figure 6(b) is the cable force signals without the influence of thermal actions, which are qualified for the following discussions.

Determination of probabilistic triggers

Data preparation for GPD discussions The length of window is a critical parameter to extract energy indices, which will influence the effectiveness of anomaly detection. If the length is short, the tolerance of energy indices for spikes is insufficient, while if the length is large, the effectiveness of anomaly detection is weakened owing to the peak clipping of anomalous
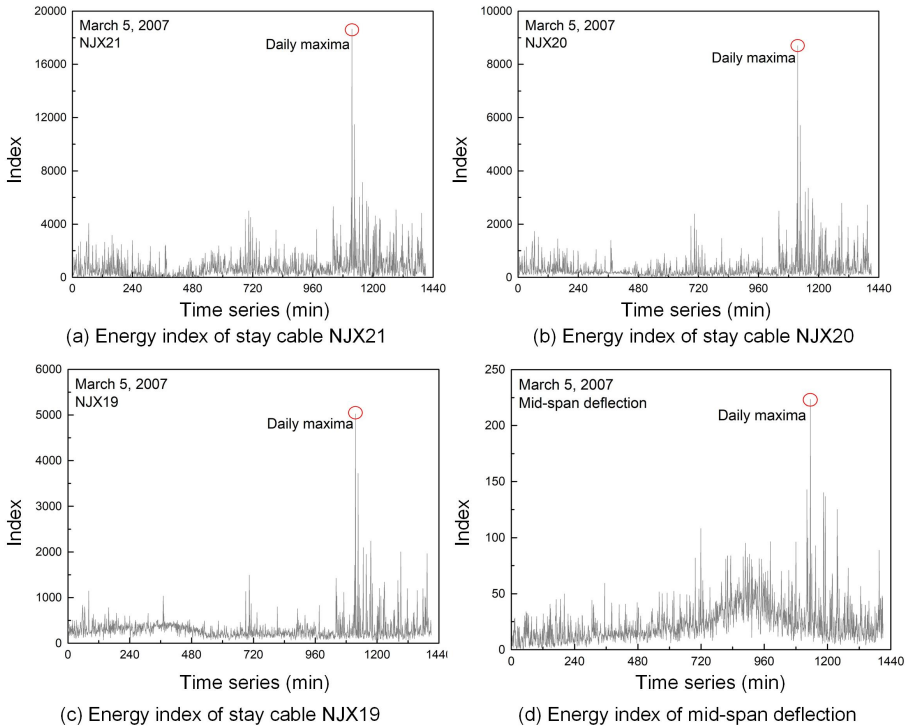
Figure 7. Extracted energy indices in 24 hours for the studied four indices.

signals. In this paper, the length of time window is determined as 60s by taking overloading events into account. The specific descriptions of the determination of window length could refer to our previous paper[27]. Considering the GPD requires samples to be independent identically distributed, none overlap is employed herein.

According to equation (1), the four energy indices along the timeline are extracted and plotted in Figure 7, where the length of time window is 60s and no overlap is applied. As requested by the GPD analysis in independent identically distribution, daily maxima, highlighted in Figure 7, are adopted for the following detection trigger estimation. The extracted daily maximum indices in 2007 are plotted in Figure 8, which are the database for the GPD discussion. A total of 245 samples in 2007 rather than 365 result from the large portion of missing data, such as one week data missing owing to electricity interruption.
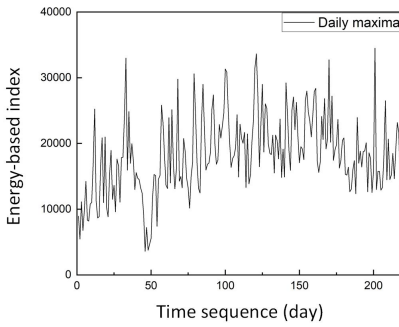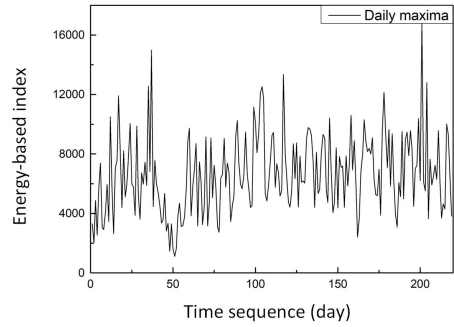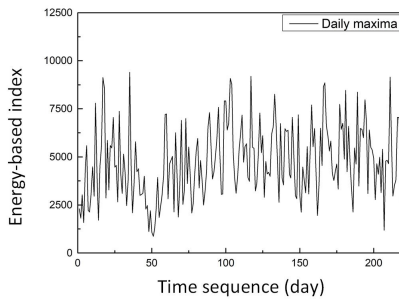
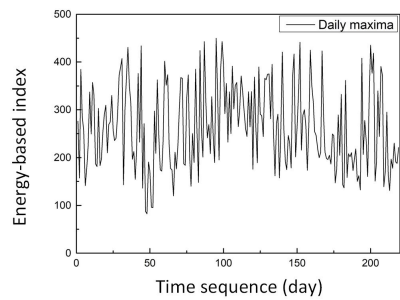**Figure 8.** Daily maxima of the energy index for the four indices in 2007.

Threshold determination To predict triggers for anomaly detection, the threshold needs to be first determined based on the characteristics of the mean excess function and RMSE. Stay cable NJX21 is taken as the example to illustrate the procedure to determine thresholds. According to equations (5) and (6), the mean excess function and RMSE derived from the daily maximum indices in 2007 are plotted in Figure 9. A potential threshold of 32,441 subject to the lowest RMSE was observed, however, when the threshold is set as 32,441, only two samples are qualified for the GPD analysis which will result in a statistical uncertainty. To lower the uncertainty, a relatively small threshold of 13,976 is adopted, which also makes mean excess function linearly related with the threshold as shown in Figure 9. Furthermore, the corresponding RMSE approaches its local lowest point, which further supports its reasonability. Therefore, the optimal threshold regarding the stay cable NJX21 for the GPD discussions is set as 13,976.
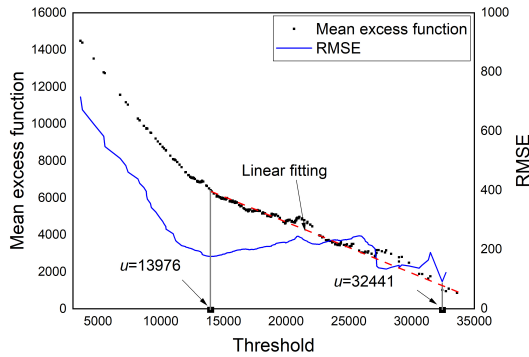
Figure 9. Mean excess function and RMSE for the daily maxma of stay cable NJX21.

Similarly, the optimal thresholds of the other three indices (i.e., cable forces of NJX20, NJX19, and mid-span deflection) are determined as 9,000, 7,000, and 420, respectively.

Bayesian estimation The stay cable NJX21 is selected to depict the procedure of Bayesian estimation. The MG sampler is used to generate the posterior distribution of the parameters, where the initial values are set as $\theta^{(0)} = (\phi^{(0)} = 6.30, \sigma^{(0)} = 1,000)$, the number of iteration $N = 40,000$, and the scale of the proposal distribution $s_\phi = 0.001, s_\sigma = 1$. The calculation results during the iteration process are shown in Figure 10, where the burn-in and stationary periods are observed. The samples within the stationary period are used to figure out the posterior distributions of the parameters. As a result, the PDFs of the two parameters are shown in Figure 11, where scale parameter $\sigma \sim N(5,965,792)$ and shape parameter $\xi \sim N(-0.1079, 0.1032)$.

Upon obtaining the posterior distributions of the parameters, the PDF of the predicted trigger is achieved. 40,000 sets of possible triggers are generated based on random scale and shape parameters. Through statistics, the PDF of predicted triggers is plotted in Figure 12(a), where the estimated triggers for force of stay cable NJX21 satisfy a Lognormal distribution, i.e., $T_a \sim LogNormal(10.8822, 0.3423)$.

Similarly, trigger distributions of the stay cables NJX20, NJX19 and mid-span deflection are obtained as shown in Figures 12(b), (c) and (d). Some critical parameters within the estimation course are listed in Table 2.
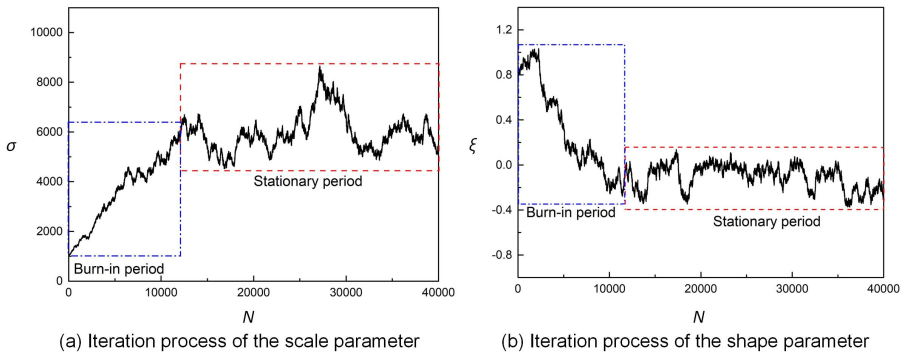
(a) Iteration process of the scale parameter   (b) Iteration process of the shape parameter

Figure 10. Iteration process of the scale and shape parameters subject to the stay cable NJX21.

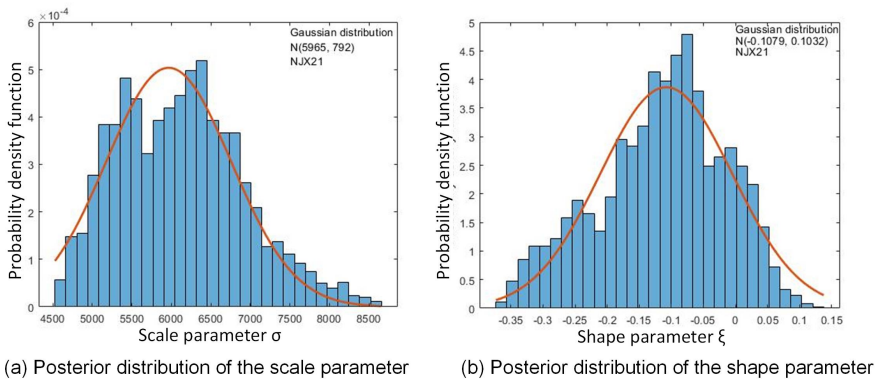(a) Posterior distribution of the scale parameter   (b) Posterior distribution of the shape parameter

Figure 11. Posterior distributions of the scale and shape parameters subject to the stay cable NJX21.

Table 2. Critical parameters within the Bayesian estimation course for the studied indices.

Index	Scale parameter	Shape parameter	Trigger
Stay cable NJX21	N(5,965, 792)	N(-0.1079, 0.1032)	LogNormal(10.882, 0.3423)
Stay cable NJX20	N(1,000, 52.5)	N(-0.0827, 0.1011)	LogNormal(9.6689, 0.1829)
Stay cable NJX19	N(585, 162)	N(-0.0381, 0.1210)	LogNormal(9.3675, 0.2382)
Mid-span deflection	N(125.3,14.4)	N(-0.014, 0.186)	LogNormal(7.3789, 0.5595)

Sensor fault detection

Owing to harsh environmental factors, sensor faults were observed gradually within the SHM system of the NDB. Through manual inspection, forces of stay cable NJX20 did not behave as expected and

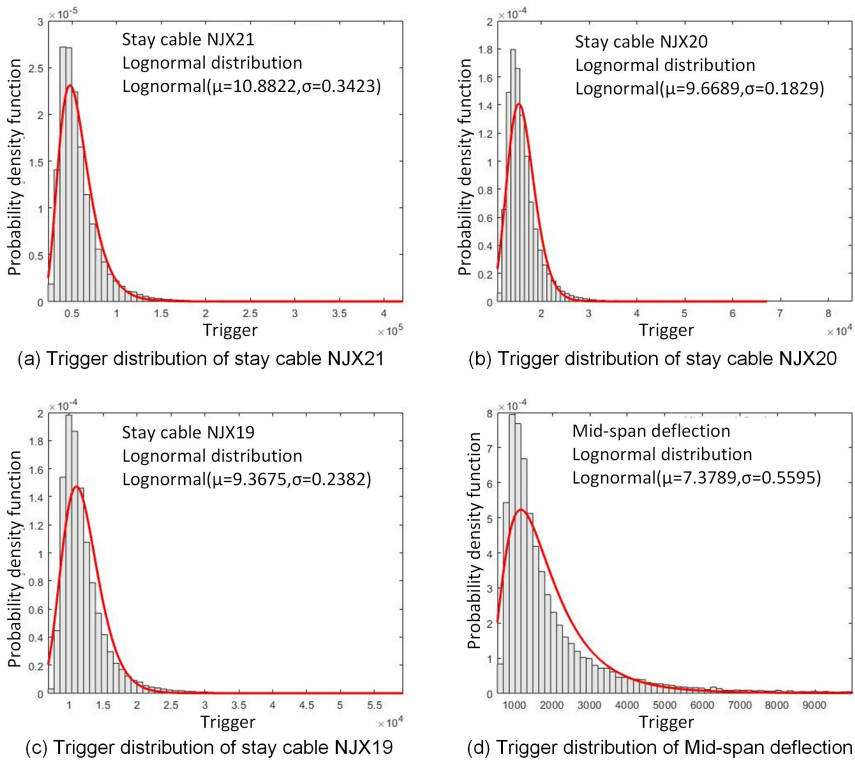**Figure 12.** Probability density function of the triggers for the four indices.

were confirmed as the failure of the anchor load cell on July 12, 2009. In detail, the measured cable force dropped from 3,600kN level to 2,500kN level as shown in Figure 13. In this regard, signals obtained from the studied four sensors on July 12, 2009 are employed for the sensor fault detection by using the proposed methodology.

Following the pre-processing procedure, the energy indices are extracted and plotted in Figure 14 based on measurements from anchor load cells of stay cables NJX21, NJX20, NJX19, and mid-span deflection sensor. According to equation (9), certainty degrees of the studied four indices are calculated accordingly and demonstrated in Figure 14.

As a result, only the index of stay cable NJX20 detects an anomalous scenario with almost 100% certainty degree, whilst the other three indices have certainty degrees of 0 which indicate the occurrence of anomaly events is almost impossible. Since the significant signal drop of the stay
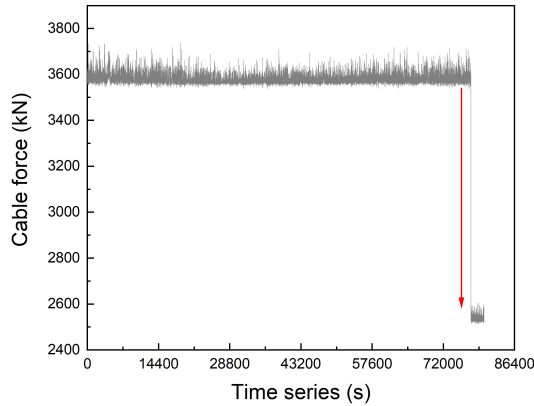
Figure 13. Forces of stay cable NJX20 on July 12, 2009 with faulty signals caused by sensor faults.

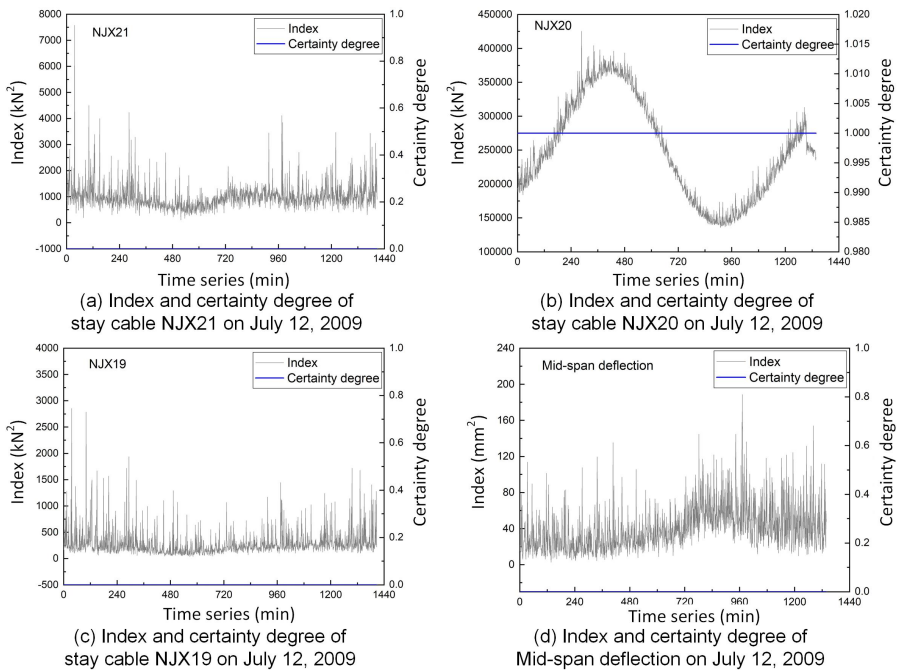**Figure 14.** Indices of the studied four sensors and their certainty degrees for sensor fault detection.

cable NJX20 destroys the period law of thermal response, tremendous errors are generated by using the multi-resolution wavelet-based thermal

response separation method, resulting in extremely high values of the energy indices.

Since the detection result of the stay cable NJX20 is against with the other three, evidential reasoning is used to form a joint one to achieve the final decision. The certainty degrees for anomaly detection subject to stay cables NJX21, NJX20, NJX19, and mid-span deflection are 0, 1, 0, 0, respectively.

In evidential reasoning, the four studied indices are regarded as four pieces of evidence. Based on the certainty degrees shown in Figure 14, the specific four pieces of evidence are expressed as

$$
\begin{aligned}
&E_1 : [m_1(A_1) = 0.00, m_1(A_2) = 1.00, m(\Gamma) = 0.00] \\
&E_2 : [m_2(A_1) = 1.00, m_2(A_2) = 0.00, m(\Gamma) = 0.00] \\
&E_3 : [m_3(A_1) = 0.00, m_3(A_2) = 1.00, m(\Gamma) = 0.00] \\
&E_4 : [m_4(A_1) = 0.00, m_4(A_2) = 1.00, m(\Gamma) = 0.00]
\end{aligned}
\tag{24}
$$

where A_1 represents anomalous events, $m(A_1)$ is the occurrence certainty degree of anomalous events, and A_2 stands for normal events, and $m(A_2)$ is the occurrence certainty degree of normal events.

According to equation (15), similarities between each two pieces of evidence are calculated and used to construct the 4×4 similarity matrix $\mathbf{R}$, which is expressed as

$$
\mathbf{R} = \begin{bmatrix} 1 & 0 & 1 & 1 \\ 0 & 1 & 0 & 0 \\ 1 & 0 & 1 & 1 \\ 1 & 0 & 1 & 1 \end{bmatrix}
\tag{25}
$$

According to equations (17) and (18), the credibility of the four pieces of evidence is (1, 0, 1, 1). Then, the collected BPA function is acquired as

$$
\begin{aligned}
&E_1 : [\hat{m}_1(A_1) = 0.00, \hat{m}_1(A_2) = 1.00, \hat{m}(\Gamma) = 0.00] \\
&E_2 : [\hat{m}_2(A_1) = 0.00, \hat{m}_2(A_2) = 0.00, \hat{m}(\Gamma) = 1.00] \\
&E_3 : [\hat{m}_3(A_1) = 0.00, \hat{m}_3(A_2) = 1.00, \hat{m}(\Gamma) = 0.00] \\
&E_4 : [\hat{m}_4(A_1) = 0.00, \hat{m}_4(A_2) = 1.00, \hat{m}(\Gamma) = 0.00]
\end{aligned}
\tag{26}
$$

According to equation (20), the relative credibility for the four pieces of evidence is (0.33, 0.00, 0.33, 0.33). Finally, according to equations (21), (22), and (23), the joint certainty degree subject to the

510 proposition of anomalous events derived from the four individual certainty
511 degrees is estimated as $m(A_1) = 0$. The anomaly detection result is
512 listed as $[m(A_1) = 0; m_1(A_1) = 0, m_2(A_1) = 1, m_3(A_1) = 0, m_4(A_1) =$
513 $0]$, which follows the mode II (i.e., sensor fault) that relatively high
514 certainty degree of a single individual index and relatively low joint
515 certainty degree. Based on this specific mode, it is concluded that the
516 anomaly is triggered by sensor faults, and the faulty sensor is the one
517 with high certainty degree of the individual index, i.e., anchor load cell
518 installed at the stay cable NJX20. The anomaly detection result by using
519 the proposed method is in line with the actual situation, which validates
520 its effectiveness.

521 *Application in snow disaster detection*

522 Nanjing city underwent a heavy snowstorm at the end of January in 2008.
523 To demonstrate the respond of the proposed anomaly detection method
524 during such extreme weather, the measurements within the snowstorm
525 time window (i.e., Jan. 26th, 2008) were discussed. The energy indices and
526 certainty degrees of the four studied sensors were collected and plotted
527 in Figure 15. The three cable force indices detect anomalous scenarios
528 with the maximum certainty degrees of 0.17(NJX21), 0.94(NJX20), and
529 0.94(NJX19), respectively. While the mid-span deflection index has a
530 certainty degree of almost 0. It is observed that the four indices performed
531 diversely in the snowstorm detection case. For instance, the indices of
532 stay cables NJX20 and NJX19 achieve a high certainty degrees for the
533 anomalous scenario, whilst the mid-span deflection index fails to detect
534 the anomaly.
535   The different performance of the four indices results from their own
536 attributes in anomaly detection. In detail, different indices have various
537 sensitivities to even the same anomalous event. In this case, the indices of
538 stay cables NJX20 and NJX19 are the most sensitive index to the anomaly
539 caused by snowstorm, while the index subject to the mid-span deflection
540 is the least. If we only use a single index, such as the mid-span deflection,
541 to detect anomalies in practice, the anomaly induced by snowstorm could
542 not be detected in this case. Thus, it is essential to use multiple indices in
543 anomaly detection to improve its efficiency.
544   To distinguish sensor faults from anomalous events, evidential reasoning
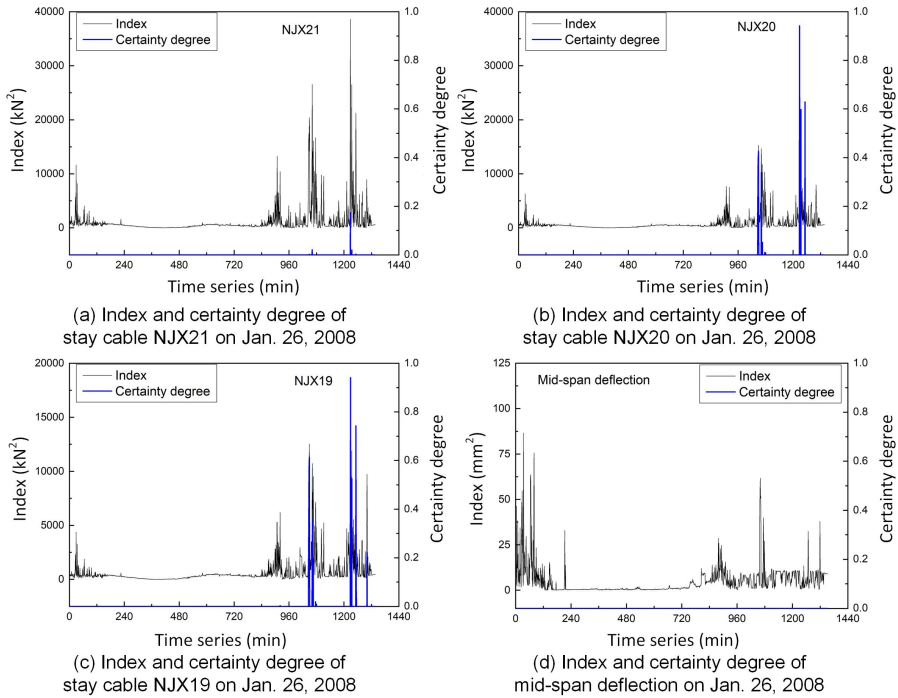545 is applied to generate the joint certainty degree. The specific calculation

Figure 15. Indices of the studied four sensors and their certainty degrees in the snowstorm detection case.

procedure of the joint certainty degree could refer to corresponding section in the sensor fault detection. As a result, the joint certainty degrees derived from the selected four indices are plotted in Figure 16. During the snow storm period (i.e., Jan. 26, 2008), anomalous scenarios are detected multiple times with various joint certainty degrees, where the maximum one is 36.82% at the $122, 8^{th}$ minute instant. The detection mode of the snowstorm is finally listed as $[m(A_1) = 36.82\%; m_1(A_1) = 17\%, m_2(A_1) = 94\%, m_3(A_1) = 94\%, m_4(A_1) = 0]$, which is in line with mode III (i.e., anomalous event) - there are multiple individual indices are triggered and the joint certainty degree is relatively high. Based on the defined modes, it is concluded that the anomaly was triggered by the snowstorm. Since a relatively high joint certainty degree of anomalous events is achieved in this case, it is suggested to pay more attention to the structural and operational conditions of the signature bridge.
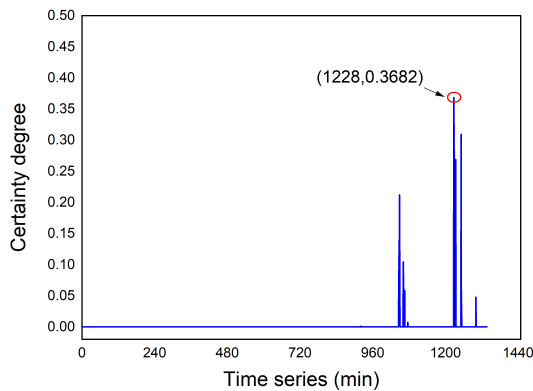
Figure 16. Joint certainty degree for the snowstorm detection on Jan. 26, 2008.

Through in-depth analysis, the fact leading to the anomalous scenario is summarized as: (I) the bridge took extra snow loads with the accumulation of snow on the pavement; and (II) since the short-term bridge shutdown generated large number of awaiting vehicles, the traffic volume was extremely large when the bridge was re-opened. Considering the structural safety, the bridge was shut down for the whole day on Jan. 27, 2008.

Discussion

In this study, an energy index in time domain is developed for anomaly detection based on pre-processed SHM measurements, which performs more robust than the single signal index, especially for signal spikes. In the signal pre-processing stage, signals are filled by using moving time window mean imputation to achieve continuity and filtered through the multi-resolution wavelet-based approach to separate thermal response.

The certainty degree, a probabilistic index for anomaly detection, is derived based on the PDF of detection triggers which is predicted by using Bayesian estimation of the GPD. In detail, MG sampler, one of MCMC algorithms, is adopted to obtain the posterior distributions of scale and shape parameters and triggers for anomaly detection.

Evidential reasoning is employed to combine multiple certainty degrees into a joint one to distinguish sensor faults from anomalous scenarios. Specifically, three detection modes are defined to tell normal operation, sensor faults and anomalous events: (I)Mode I - Both individual and joint indices are 0 or extremely low; (II) Mode II - Relatively high single

individual index together with a relatively low joint index, and the faulty sensor is subject to the relatively high single index; and (III) Mode III - Multiple relatively high individual indices and relatively high joint index.

The effectiveness of the multi-index probabilistic anomaly detection methodology is verified by using field measurements from the NDB. Sensor fault detection and snow disaster detection are presented in this study. The sensor fault is detected as mode II (i.e., sensor fault) - a nearly 0 joint certainty degree and an almost 100% certainty degree of stay cable NJX20, which indicates the probability of the failure of the anchor load cell at the stay cable NJX20 is extremely high. Furthermore, the snow disaster is detected as mode III (anomalous event) - a 36.82% joint certainty degree. It is suggested to pay more attention to the structural and operational safety of the signature bridge.

Conclusions

In this paper, a multi-index probabilistic anomaly detection method is developed for large span bridges to rate the uncertainties within the detection course and distinguish sensor faults from anomalous scenarios. The Bayesian estimation of GPD is capable to model the uncertainties within the detection process, where a probabilistic index, i.e., certainty degree, is defined to describe the occurrence probability of anomalous events. In addition, evidential reasoning could distinguish sensor faults from anomalous scenarios by incorporating multiple probabilistic detection results into a joint one, where three modes are defined corresponding to normal operation, sensor fault and anomalous scenario, respectively.

Since the proposed method is on the foundation of the assumption that anomalous scenarios will trigger multiple indices, it is challenge to distinguish sensor faults from localized damages. In addition, no such localized damages are observed in field, and the proposed model cannot simulate localized damages. It is suggested to establish localized damage models in the future or record actual monitored localized signals to carry out further studies. It is recommended to distinguish localized damages from sensor faults by different detection modes based on the particular obtained localized damage information.

The proposed model could raise alerts when the structure facing sudden threats. However, the remaining life of the bridge cannot be estimated

by using the model. After alert, owners should organize inspection and assessment tasks to ensure the safety of the bridge. In the future, the method to predict remaining life of bridge should be studied based on inspection information.

Acknowledgements

References

1. Rohan A, Raouf I and Kim HS. Rotate vector (RV) reducer fault detection and diagnosis system: Towards component level prognostics and health management (PHM). *Sensors* 2020; 20(23): 6845.

2. Khan A, Khalid S, Raouf I et al. Autonomous assessment of delamination using scarce raw structural vibration and transfer learning. *Sensors* 2021; 21(18): 6239.

3. Fujino Y, Siringoringo DM, Ikeda Y et al. Research and implementations of structural monitoring for bridges and buildings in Japan. *Engineering* 2019; 5(6): 1093–1119.

4. Xu YL and Xia Y. *Structural health monitoring of long-span suspension bridges*. CRC Press, 2019.

5. Ou J and Li H. Structural health monitoring in mainland China: review and future trends. *Structural Health Monitoring* 2010; 9(3): 219–231.

6. Pandey A, Biswas M and Samman M. Damage detection from changes in curvature mode shapes. *Journal of Sound and Vibration* 1991; 145(2): 321–332.

7. Salawu O. Detection of structural damage through changes in frequency: a review. *Engineering Structures* 1997; 19(9): 718–723.

8. Das S, Saha P and Patro S. Vibration-based damage detection techniques used for health monitoring of structures: a review. *Journal of Civil Structural Health Monitoring* 2016; 6(3): 477–507.

9. Peeters B, Maeck J and De Roeck G. Vibration-based damage detection in civil engineering: excitation sources and temperature effects. *Smart Materials and Structures* 2001; 10(3): 518–527.

10. Xu ZD and Wu Z. Simulation of the effect of temperature variation on damage detection in a long-span cable-stayed bridge. *Structural Health Monitoring* 2007; 6(3): 177–189.

11. Yu Z, Xia H, Goicolea JM et al. Bridge damage identification from moving load induced deflection based on wavelet transform and Lipschitz exponent. *International Journal of Structural Stability and Dynamics* 2016; 16(05): 1550003.

12. Hua X, Ni Y, Chen Z et al. Structural damage detection of cable-stayed bridges using changes in cable forces and model updating. *Journal of Structural Engineering* 2009; 135(9): 1093–1106.

13. Ren Y, Xu X, Huang Q et al. Long-term condition evaluation for stay cable systems using dead load–induced cable forces. *Advances in Structural Engineering* 2019; 22(7): 1644–1656.

14. Kromanis R and Kripakaran P. Predicting thermal response of bridges using regression models derived from measurement histories. *Computers & Structures* 2014; 136: 64–77.

15. Xu X, Ren Y, Huang Q et al. Thermal response separation for bridge long-term monitoring systems using multi-resolution wavelet-based methodologies. *Journal of Civil Structural Health Monitoring* 2020; 10(3): 527–541.

16. Wu1a B and Li Z. Multiscale features and information extraction of online strain for long-span bridges. *Smart Structures and Systems* 2014; 14(4): 679–697.

17. Zhu Y, Ni YQ, Jesus A et al. Thermal strain extraction methodologies for bridge structural condition assessment. *Smart Materials and Structures* 2018; 27(10): 105051.

18. Xu X, Huang Q, Ren Y et al. Modeling and separation of thermal effects from cable-stayed bridge response. *Journal of Bridge Engineering* 2019; 24(5): 04019028.

19. Zhou Y and Sun L. A comprehensive study of the thermal response of a long-span cable-stayed bridge: from monitoring phenomena to underlying mechanisms. *Mechanical Systems and Signal Processing* 2019; 124: 330–348.

20. Wang H, Zhang YM, Mao JX et al. Modeling and forecasting of temperature-induced strain of a long-span bridge using an improved Bayesian dynamic linear model. *Engineering Structures* 2019; 192: 220–232.

21. Ni Y, Wang Y and Zhang C. A Bayesian approach for condition assessment and damage alarm of bridge expansion joints using long-term structural health monitoring data. *Engineering Structures* 2020; 212: 110520.

22. Xu X, Ren Y, Huang Q et al. Anomaly detection for large span bridges during operational phase using structural health monitoring data. *Smart Materials and Structures* 2020; 29(4): 045029.

23. Zhu Y, Ni YQ, Jin H et al. A temperature-driven MPCA method for structural anomaly detection. *Engineering Structures* 2019; 190: 447–458.

24. Tomé ES, Pimentel M and Figueiras J. Damage detection under environmental and operational effects using cointegration analysis–application to experimental data from a cable-stayed bridge. *Mechanical Systems and Signal Processing* 2020; 135: 106386.

25. Fan ZY, Huang Q, Ren Y et al. A cointegration approach for cable anomaly warning based on structural health monitoring data: An application to cable-stayed bridges. *Advances in Structural Engineering* 2020; 23(13): 2789–2802.

26. Huang HB, Yi TH, Li HN et al. Strain-based performance warning method for bridge main girders under variable operating conditions. *Journal of Bridge Engineering* 2020; 25(4): 04020013.

27. Xu X, Qian ZD, Huang Q et al. Probabilistic anomaly trend detection for cable-supported bridges using confidence interval estimation. *Advances in Structural Engineering* 0; 0(0):

13694332211056108.

28. Yu Y and Cai C. Prediction of extreme traffic load effects of bridges using Bayesian method and application to bridge condition assessment. *Journal of Bridge Engineering* 2019; 24(3): 04019003.

29. Xu X, Forde MC, Ren Y et al. A Bayesian approach for site-specific extreme load prediction of large scale bridges. *Structure and Infrastructure Engineering* 2021; : 1–14.

30. Huang HB, Yi TH and Li HN. Sensor fault diagnosis for structural health monitoring based on statistical hypothesis test and missing variable approach. *Journal of Aerospace Engineering* 2017; 30(2): B4015003.

31. Xu X, Huang Q, Ren Y et al. Sensor fault diagnosis for bridge monitoring system using similarity of symmetric responses. *Smart Structures and Systems* 2019; 23(3): 279–293.

32. Kullaa J. Distinguishing between sensor fault, structural damage, and environmental or operational effects in structural health monitoring. *Mechanical Systems and Signal Processing* 2011; 25(8): 2976–2989.

33. Tang Z, Chen Z, Bao Y et al. Convolutional neural network-based data anomaly detection method using multiple information for structural health monitoring. *Structural Control and Health Monitoring* 2019; 26(1): e2296.

34. Huang HB, Yi TH and Li HN. Anomaly identification of structural health monitoring data using dynamic independent component analysis. *Journal of Computing in Civil Engineering* 2020; 34(5): 04020025.

35. Kalaycioglu O, Copas A, King M et al. A comparison of multiple-imputation methods for handling missing data in repeated measurements observational studies. *Journal of the Royal Statistical Society Series A (Statistics in Society)* 2016; 179(3): 683–706.

36. Nevalainen J, Kenward MG and Virtanen SM. Missing values in longitudinal dietary data: a multiple imputation approach based on a fully conditional specification. *Statistics in Medicine* 2009; 28(29): 3657–3669.

37. Ni Y, Xia H, Wong K et al. In-service condition assessment of bridge deck using long-term monitoring data of strain response. *Journal of Bridge Engineering* 2012; 17(6): 876–885.

38. Hawthorne G, Hawthorne G and Elliott P. Imputing cross-sectional missing data: comparison of common techniques. *Australian & New Zealand Journal of Psychiatry* 2005; 39(7): 583–590.

39. Enders CK. A primer on maximum likelihood algorithms available for use with missing data. *Structural Equation Modeling* 2001; 8(1): 128–141.

40. Martinez-Luengo M, Shafiee M and Kolios A. Data management for structural integrity assessment of offshore wind turbine support structures: data cleansing and missing data imputation. *Ocean Engineering* 2019; 173: 867–883.

41. Lai WY and Kuok K. A study on Bayesian principal component analysis for addressing missing rainfall data. *Water Resources Management* 2019; 33(8): 2615–2628.

42. Hera A and Hou Z. Application of wavelet approach for ASCE structural health monitoring benchmark studies. *Journal of Engineering Mechanics* 2004; 130(1): 96–104.

43. Xia YX and Ni YQ. A wavelet-based despiking algorithm for large data of structural health monitoring. *International Journal of Distributed Sensor Networks* 2018; 14(12): 1550147718819095.

44. Liu Y, Deng Y and Cai C. Deflection monitoring and assessment for a suspension bridge using a connected pipe system: a case study in China. *Structural Control and Health Monitoring* 2015; 22(12): 1408–1425.

45. Ding Y, Zhou G, Li A et al. Thermal field characteristic analysis of steel box girder based on long-term measurement data. *International Journal of Steel Structures* 2012; 12(2): 219–232.

46. Deng Y, Li A, Liu Y et al. Investigation of temperature actions on flat steel box girders of long-span bridges with temperature monitoring data. *Advances in Structural Engineering* 2018; 21(14): 2099–2113.

47. Xu X, Xu YL, Ren Y et al. Site-specific extreme load estimation of a long-span cable-stayed bridge. *Journal of Bridge Engineering* 2021; 26(4): 05021001.

48. Zhou GD, Yi TH, Chen B et al. A generalized Pareto distribution–based extreme value model of thermal gradients in a long-span bridge combining parameter updating. *Advances in Structural Engineering* 2017; 20(2): 202–213.

49. Liu Q and Tong XT. Accelerating Metropolis-within-Gibbs sampler with localized computations of differential equations. *Statistics and Computing* 2020; 30(4): 1037–1056.

50. Bi W, Zhang A and Yuan Y. Combination method of conflict evidences based on evidence similarity. *Journal of Systems Engineering and Electronics* 2017; 28(3): 503–513.

51. Xiao F. A new divergence measure for belief functions in D–S evidence theory for multisensor data fusion. *Information Sciences* 2020; 514: 462–483.

52. Zhang Z, Liu T and Zhang W. Novel paradigm for constructing masses in Dempster-Shafer evidence theory for wireless sensor network's multisource data fusion. *Sensors* 2014; 14(4): 7049–7065.

53. Guo K and Li W. Combination rule of D–S evidence theory based on the strategy of cross merging between evidences. *Expert Systems with Applications* 2011; 38(10): 13360–13366.

54. Yager RR. On the Dempster-Shafer framework and new combination rules. *Information Sciences* 1987; 41(2): 93–137.

55. Murphy CK. Combining belief functions when evidence conflicts. *Decision Support Systems* 2000; 29(1): 1–9.